JOURNAL OF SYNCHROTRON RADIATION

ISSN 1600-5775

The LCLS variable-energy hard X-ray single-shot spectrometer

David Rich,* Diling Zhu, James Turner, Dehong Zhang, Bruce Hill and Yiping Feng*

Linac Coherent Light Source, SLAC National Accelerator Laboratory, 2575 Sand Hill Road, Menlo Park, CA 94025, USA. *Correspondence e-mail: drich@slac.stanford.edu, yfeng@slac.stanford.edu

Received 11 November 2015
Accepted 25 November 2015

Edited by M. Zangrando, IOM-CNR and Elettra-Sincrotrone, Italy

Keywords: spectrometer; X-ray; free-electron laser (FEL); variable energy; single shot; transmissive; bent thin crystal.

The engineering design, implementation, operation and performance of the new variable-energy hard X-ray single-shot spectrometer (HXSSS) for the LCLS free-electron laser (FEL) are reported. The HXSSS system is based on a cylindrically bent Si thin crystal for dispersing the incident polychromatic FEL beam. A spatially resolved detector system consisting of a Ce:YAG X-ray scintillator screen, an optical imaging system and a low-noise pixelated optical camera is used to record the spectrograph. The HXSSS provides single-shot spectrum measurements for users whose experiments depend critically on the knowledge of the self-amplified spontaneous emission FEL spectrum. It also helps accelerator physicists for the continuing studies and optimization of self-seeding, various improved mechanisms for lasing mechanisms, and FEL performance improvements. The designed operating energy range of the HXSSS is from 4 to 20 keV, with the spectral range of order larger than 2% and a spectral resolution of 2×10^{-5} or better. Those performance goals have all been achieved during the commissioning of the HXSSS.

1. Introduction

The stochastic nature of the self-amplified spontaneous emission (SASE) lasing process (Kondratenko & Saldin, 1979; Bonifacio *et al.*, 1984) gives rise to pulse-to-pulse fluctuations in all physical attributes of X-ray free-electron laser (FEL) beams, including the spectral content. Many techniques have been developed to capture the pulse-to-pulse FEL spectrum (Brenner *et al.*, 2011; Svetina *et al.*, 2011; Inubushi *et al.*, 2012; Zhu *et al.*, 2012, Karvinen *et al.*, 2012, Makita *et al.*, 2015). The method of using a thin bent Si crystal to spectrally disperse the hard X-ray FEL beam was first demonstrated at the Linac Coherent Light Source (LCLS) in late 2011 (Zhu *et al.*, 2012; Feng *et al.*, 2012). The in-air prototype setup installed in the X-ray pump probe (XPP) instrument was an essential diagnostic in establishing the LCLS hard X-ray self-seeding (Amann *et al.*, 2012). Increased demand for spectral beam diagnostics led to the expedited R&D project to build and install an 8.4 keV fixed-energy spectrometer inside the LCLS front-end enclosure (FEE) immediately downstream of the undulators (Rich *et al.*, 2012). It was frequently used in subsequent seeding studies and other new FEL capability development activities. A dual crystal upgrade (Rich *et al.*, 2013) to operate at three different photon energies 4.5, 8.4 and 9.1 keV was implemented the following year, with the 4.5 keV configuration specifically included to enable the studies of potential terawatt FEL performance (Wu & Feng, 2014) because the FEL gain length at 4.5 keV is shorter so strong tapering can be applied post-saturation given the limited total

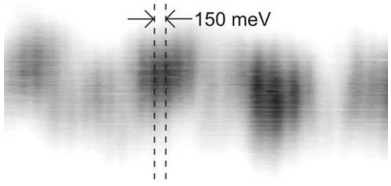

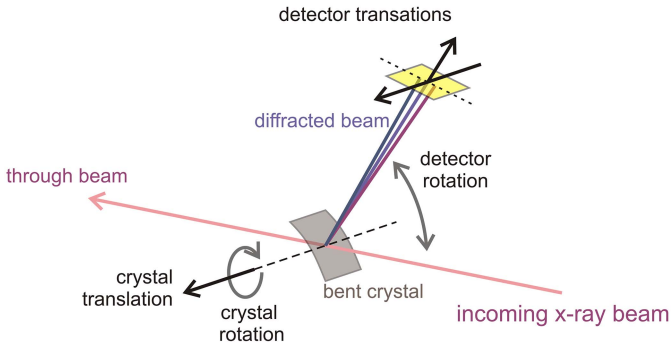

Figure 1
Schematic of the LCLS variable-energy hard X-ray spectrometer, which consists of a bent thin (10–20 μm) crystal, a Ce:YAG single-crystal X-ray scintillating screen, and an optical lens and a pixelated camera (not shown). There are five degrees of freedom in various corresponding motions for performing energy tuning and other optimizations.

length of the LCLS undulator system. In late 2014, a variable-energy hard X-ray spectrometer with an operating range from 4 keV to 20 keV was designed and installed in the FEE at the same location and replaced the fixed-energy spectrometer. In this article, we describe the design, implementation, operation and performance of this variable-energy spectrometer.

The operational principle of the bent-crystal spectrometer has been described previously (Zhu *et al.*, 2012; Feng *et al.*, 2012). The basic geometry and degrees of motion freedom are schematically shown in Fig. 1. A polychromatic but highly collimated FEL beam impinges on a bent thin single crystal of the material of choice with its curvature aligned in the vertical plane. As different horizontal slices of the beam make different incidence angles with respect to the local diffraction planes, only one within a given slice would satisfy the Bragg condition, and thus is diffracted out at a different exit angle. The diffracted beams from different slices collectively form an angularly dispersed spectrograph, which in turn can be mapped onto a (flat) spatial spectrograph if the detector is positioned at a sufficient distance away.

The bent-crystal spectrometer offers several advantages. First of all, it can be used as a diagnostic for monitoring the random FEL spectrum because it is highly transmissive operating at typical hard X-ray energies. It is one of the most efficient spectral measurement methods; other than the loss associated with photoabsorption, all diffracted X-rays contribute towards the spectral signal. High Miller indices can be used to achieve sufficiently high resolution to resolve the spectral spikes (Saldin *et al.*, 1998) in a SASE FEL beam. Finally, single-shot measurement speed is only limited by the readout speed of the optical imaging camera, which has seen continuous improvement by industrial development.

2. Specification and design considerations

The superb performance of the LCLS first-generation spectrometer even when limited to a fixed energy has enabled a number of important new FEL capability developments (Marinelli *et al.*, 2013; Lutman *et al.*, 2014), and increasingly users and FEL operators alike were seeking the flexibility to work at different energies and with different spectral resolution and range. For example, the study of the detailed longitudinal properties of the beam requires the highest possible energy resolution; two-color SASE operations require an energy range as large as 200–300 eV with ∼1 eV resolution; the few- to sub-femtosecond FEL development asks for sensitivity at the μJ level because of low pulse energy. A follow-on LCLS X-ray improvement project was undertaken to address these needs by replacing the fixed-energy spectrometer with a variable-energy hard X-ray single-shot spectrometer (HXSSS) at the same location to serve all hard X-ray hutches. It was required to provide non-invasive measurement during user operation to the extent feasible, and to cover the full SASE spectrum with better than 1 eV resolution at the maximum LCLS repetition rate of 120 Hz. In addition, the physics requirements included:

(*a*) Covering a full hard X-ray operating range from 4 to 20 keV.

(*b*) Option of providing up to 50000 resolving power (0.16 eV at 8 keV).

(*c*) Option of providing up to 2% spectral range.

(*d*) Having sufficient sensitivities allowing for advanced machine development with ultra-low FEL output (approximately 1 μJ).

(*e*) Providing greater than 50% transmission of the incident beam intensity.

The variable-energy HXSSS system is shown in detail in Fig. 2: a drawing of the side view (Fig. 2*a*), a drawing of the view in the direction of the beam (Fig. 2*b*) and a photograph of the overall installation (Fig. 2*c*). The physics requirements

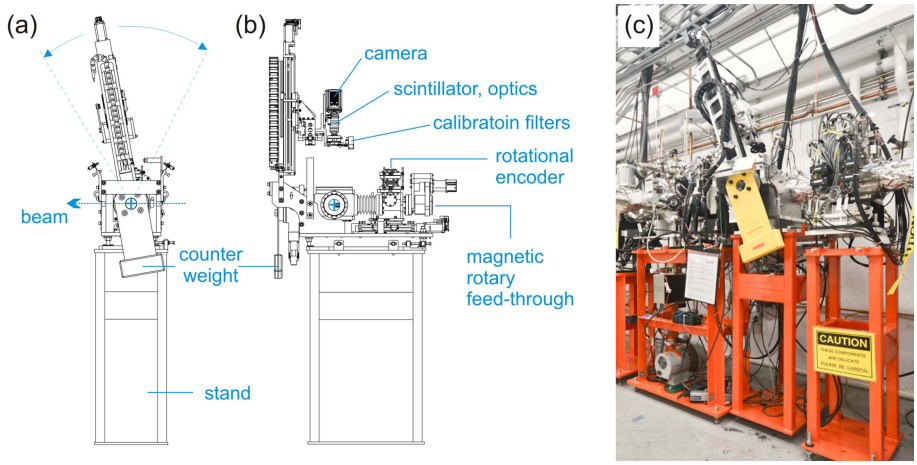

Figure 2
Pictorial detail of the LCLS variable-energy hard X-ray single-shot spectrometer. (*a*) Side view with the FEL beam propagating from right to left; (*b*) view in the direction of the beam; and (*c*) the installed variable-energy HXSSS in the LCLS FEE.

have led to many engineering design considerations. The variable-energy capability required the concentric rotation of both the crystal and the detector. Owing to the close proximity of the spectrometer to the LCLS hard X-ray offset mirror systems (HOMS), there were concerns about possible contamination, and it was chosen that all actuation and positioning devices need to be kept out of vacuum. The in-vacuum motions of the crystal, including both the θ rotation for energy tuning and the horizontal translation for swapping crystals of different orientations, were achieved by using a bellow to allow translation and a magnetic rotary drive feed-though for rotation as illustrated in Fig. 2(*b*). The magnetic feed-through uses a thin metal membrane to completely separate the vacuum and thus relies on indirect coupling, but is advantageous over other direct coupling solutions using ferrofluids in minimizing the risk of potential vacuum leaks. An in-vacuum absolute rotary encoder was utilized to accurately measure the crystal angle to mitigate potential slippage between the out-of-vacuum drive and the in-vacuum rotational shaft.

The 2θ rotation of the detector assembly was concentric to that of θ, with a total angular range of 60° from 60 to 120° due to space limitation in the FEE especially along the beam direction, as can be seen from Fig. 2(*c*). The detector assembly, including a Ce:YAG scintillator and an imaging camera, was mounted on a relatively short arm of 500 mm in length with a counter weight on the opposite side. This arrangement would have been almost impractical without using X-ray scintillation and optical imaging that afforded a much more compact system because of the very small pixel sizes (∼5 µm) of the optical camera. A state-of-the-art X-ray camera capable of running at a 120 Hz frame rate typically has pixel sizes of order 50–100 µm, and for an equal angular spectral dispersion it would have had to be positioned at least 5 m from the crystal. To partially compensate for the loss of the detection efficiency, a current state-of-the-art fast optical camera (Hamamatsu Orca Flash4.0) based on the SciCMOS technology was chosen, which has a very low readout noise[1] of order of a few e^- RMS, about a factor of ten improvement compared with the Adimec OPAL-1000 CCD camera used for the previous fixed-energy spectrometer at LCLS. The bit-depth of 16 from the Orca *versus* 12 from the OPAL also offered additional dynamics range. In addition, a large numerical aperture (NA) lens system with a motorized iris was used in place of the previous variable zoom lens to increase the effective dynamic range of detection. A dynamic range of 20000 from the Orca camera in combination with the more than 100× adjustability of the iris led to an overall dynamic range of the imaging system to be well beyond 10^6. To change the angular field-of-view of the spectrograph in the camera, the distance between the Ce:YAG screen and the thin crystals can be adjusted. The removal of the variable zoom lens provided another factor of ten increase in signal-to-noise ratio (SNR). The frame rate of the camera can be configured to run up to the maximum LCLS repetition rate of 120 Hz by selecting a smaller and rectangular region of interest (2048 × 400). Single-shot spectra can be captured, processed and transferred across the LCLS data acquisition network as part of the synchronous user data stream. Typically, a projection (summation) is often made in the direction perpendicular to the dispersion to generate (line) spectra of considerably less data volume.

The dispersed beam exits the vacuum chamber through a beryllium (Be) window at different angles depending on the photon energy and the crystal reflections selected. The thickness of the Be window (250 µm thick) was optimized to be as thin as possible but thick enough to sustain the vacuum forces to allow for a sufficiently large size to cover the angular spread of the dispersed beam as required by the operating photon energy range. This optimization was helped by the fact that the dispersion happens only in the vertical plane and the Be window could assume a rectangular shape of a very large aspect ratio. However, the maximum available size of the Be window still entailed that it had to be positioned relatively close to the crystal, leaving a long air path in between the window and the Ce:YAG screen as shown in Fig. 2(*b*). This implementation compromise could potentially degrade the fidelity of the dispersed beam, although it appeared that any effect of diffuse scattering or coherent speckles from the window did not impact on the spectral measurements significantly (per discussion of spectrometer performances in §3).

As the variable-energy HXSSS is located upstream of the LCLS hard X-ray offset mirror system, there is non-FEL radiation, such as the undulator spontaneous radiation, incident on the spectrometer crystal. These X-rays are far from being collinear with the FEL beam and do not disperse in accordance with the dispersion relation established for a highly collimated incident beam (Zhu *et al.*, 2012; Feng *et al.*, 2012), thus making spurious contribution to the real spectral signals. In early commissioning of the fixed-energy spectrometer, less clean spectra were observed as compared with the ones obtained at locations further downstream of the HOMS mirrors (Rich *et al.*, 2012). Dedicated slits were added upstream of the crystal to clean up the captured spectrographs.

To potentially accommodate a very diverse set of use cases in the operating photon energy, spectral range and resolution, and given the limited angular motion range of 60° for the 2θ arm, we have included in the design multiple crystals of various orientations with several bending radii of curvature. Depending on the exact operating parameters, the best combination crystal orientation and the bending radius is selected after trade-off considerations are made. As shown in Figs. 3(*a*) and 3(*b*), the 2θ angles of the Bragg diffraction for various crystal orientations are plotted as a function of the photon energy for silicon and diamond, respectively. The horizontal dashed lines represent the boundary defined by the designed angular motion range of the 2θ arm from 60° to 120°. To cover the photon energy range from 4 to 20 keV, three silicon crystals of (111), (220) and (100) cuts with six usable reflections (111), (333), (555), (400), (220) and (440) for silicon could be used, and similarly for diamond. In the end, only two

[1] For FEL applications, the dark noise in the camera usually does not contribute significantly because of the integration time being set possibly at a few milliseconds level if a global shutter is available. For cameras using a rolling shutter, dark noise contributions must be considered.

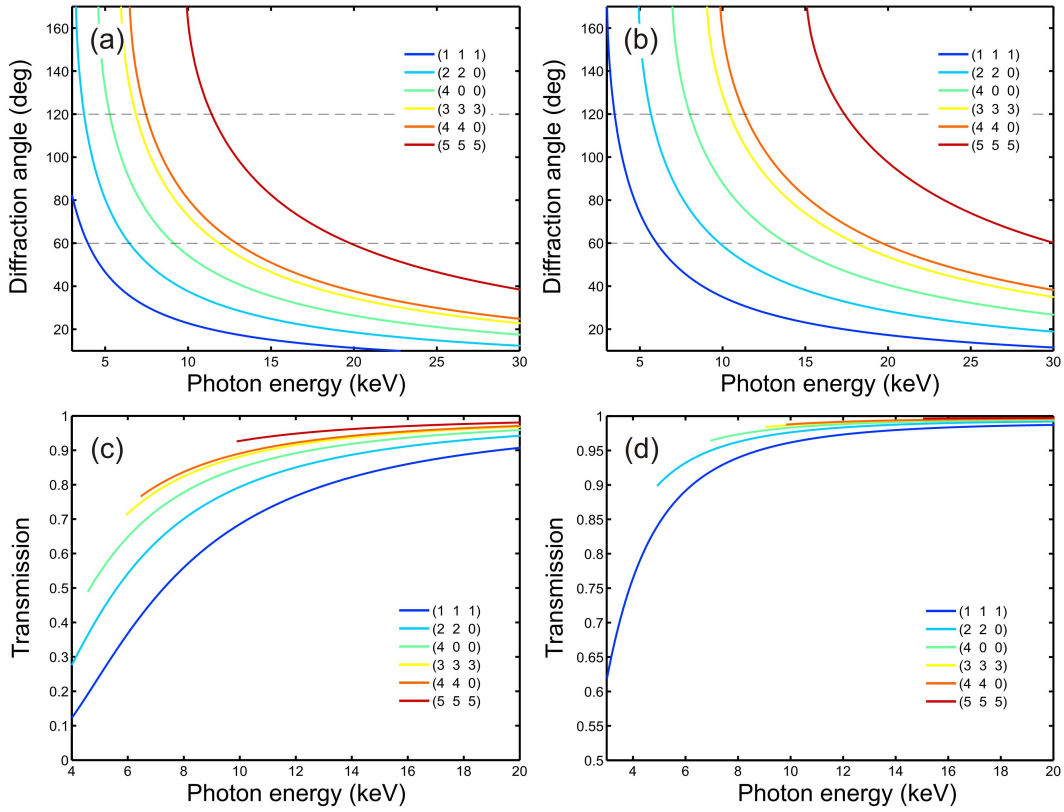

Figure 3
(*a*, *b*) 2θ angles of the Bragg diffraction with the various crystal orientations for silicon and diamond, respectively. The horizontal dashed lines represent the boundary defined by the designed angular motion range of the detector arm. (*c*, *d*) Transmissions of the spectrometer assuming a silicon crystal of 10 µm thickness or a diamond crystal of 20 µm thickness.

silicon crystals of (220) and (100) cuts were installed, and the (220), (440) and (400) reflections were sufficient to cover from 4 to 11 keV photon energy, and the (800) reflection for photon energy up to 19.5 keV. The transmission for the various reflections is plotted in Figs. 3(*c*) and 3(*d*) for 10 µm-thick silicon and 20 µm-thick diamond crystals, respectively.

The spectral range is also a very important parameter to optimize because of the relatively broad SASE bandwidth of the order of 1% including jitter in the central wavelength, depending on the FEL operating conditions such as the degree of compression of the electron bunch. For the bent-crystal spectrometer, the spectral range is directly proportional to the beam size in the plane of dispersion and inversely proportional to the radius of curvature. Given the location of the spectrometer and the FEL beam divergence, an optimal radius of curvature can be calculated for a required spectral range. In Fig. 4, the radii of curvature are plotted as a function of the Bragg angle θ for typical beam sizes of 150, 300 and 500 µm in the FEE over the required photon energy range. To cover the 30–60° angular range, a radius of curvature of ∼10 mm must be used to achieve the 1% spectral range if the beam size is only 150 µm. To cover a 2% spectral range, even smaller radii must be used. Typically, the smaller Bragg angle side of the range was used for large-range applications and the higher angles side more optimized for higher resolution focusing on only a portion of the spectrum.

The small magnitude of the required radius of curvature at large Bragg angles can introduce the unintended consequence of reduced spectral resolution. The lattice spacing of the crystal decreases from the outermost layers to the inner ones because of bending and thus smearing the resolution. The smaller the radius is, the bigger the reduction in resolution. This can be mitigated by using thinner crystals down to of the

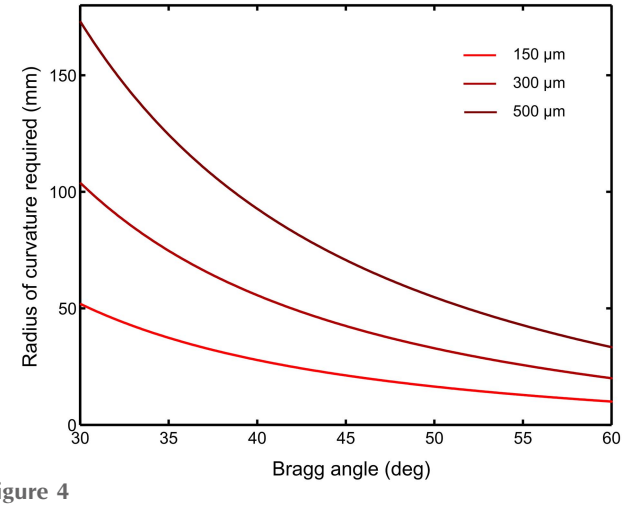

Figure 4
Bending requirement, in millimetres, as a function of the Bragg angle assuming a 1% spectral range, for three different beam sizes.

order of the extinction depth of the chosen reflections. Further reduction in crystal thickness would then lead to the intrinsic broadening as a result of too few lattice planes. We chose 50 mm and 100 mm radii based on experimental observation of the reduction in resolution at radius values close to 20–30 mm. Achieving large spectral range and high spectral resolution at the same time thus requires careful balance between the choice of the crystal reflection, the crystal thickness and the bend radius.

The variability of the new HXSSS in the operating photon energy range required energy calibration capability not available previously on the fixed-energy devices. Energy calibration is accomplished by using various absorption foils which can be inserted before the Ce:YAG X-ray scintillation screen as depicted in Fig. 2(*b*). This would enable the energy calibration at the well spaced *K*-edges across the whole operation range and allow the intermediate energy positions to be interpolated.

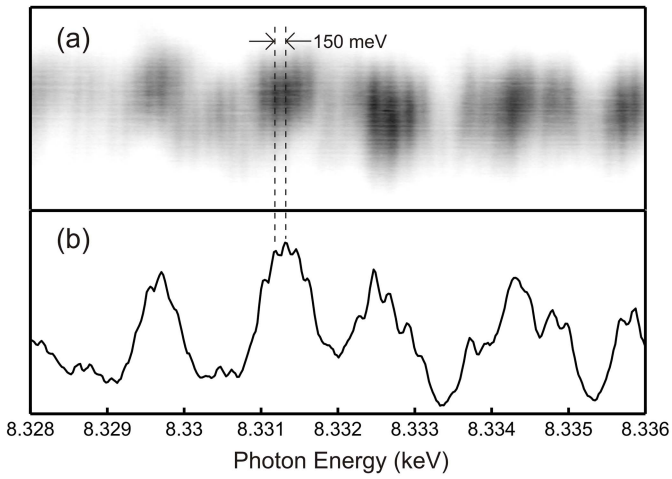

Figure 5
Detail of a typical spectrograph (*a*) of a SASE beam and its projection (*b*) recorded using the Si (440) reflection at 8.33 keV. Spectral fringes with spacing of −150 meV were well resolved, corresponding to a resolving power of 5.6×10^4.

3. Commissioning, operation and performance

The commissioning of the HXSSS was focused on characterizing the geometric imperfection of the device in order to build up a calibration table to allow 'turn-key' operation. We first conducted photon energy calibrations using the standard foils in front of the scintillator screen. This procedure needs to be performed at various detector (camera) distances to correct for the remaining alignment error of the translation stage of the detector. Knowing the exact photon energy also allows the calibration of all crystallographic miscut as well as crystal concentricity errors. We performed these procedures at the transition metal *K*-edges of Fe (7.11 keV), Ni (8.33 keV) and Cu (8.99 keV) for each of the installed crystals. Control software was developed to integrate these calibration values and interpolate/extrapolate the correct motor positions across the whole operation energy range. The absolute accuracy of the calibration was estimated to better than 5 eV across the whole operation range. A control interface was made for the users to take the crystal/crystalline indices and the photon energy as the basic input and drive the crystal, the detector arm and the camera to their respective positions. The GUI also shows important parameters of the target setup such as energy range, eV pixel^{-1} estimation, damage threshold, *etc*. After completion of the calibration, the spectrometer insertion and alignment typically takes only a few minutes.

The achieved spectral resolution of the HXSSS was demonstrated using the Si (440) reflection of a 10 µm crystal bent to 100 mm in radius with the detector/scintillator positioned at a maximum of 500 mm. As can be seen from Fig. 5, fine spectral lines were well resolved and in this case the smallest fringe spacing was ∼150 meV at 8.33 keV, or a resolving power greater than 5.6×10^4. The fringe spacing is already very close to the intrinsic spectral width of the SASE spikes at 130 meV for a 25 fs long flat-top FEL pulse (Saldin *et al.*, 1998) and is comparable with that reported previously (Zhu *et al.*, 2012), although the fringe contrast observed here was somewhat lower.

Another important question is how similar is the measured spectrum in FEE compared with the actual X-ray spectrum that arrives at the sample. This is particularly important owing to the fluctuations of the SASE FEL beam properties in combination with the various optics and diagnostic components in between the spectrometer and the sample. For this purpose we cross-compared the spectral measurements at the XPP instrument against those using the FEE HXSSS. A separate Si (220) spectrometer was set up in XPP at the potential sample location. A typical example is shown in Fig. 6. One can see that the spectrograph taken from the XPP spectrometer has additional streaks in the (horizontal) direction normal to the dispersion. These horizontal streaks were a result of the surface imperfections and slope errors of the HOMS mirrors. In addition, a portion of beam was clipped due to the FEL beam footprint being larger than the horizontal acceptance of the HOMS system. Taking these into consideration, the small disagreement between the FEE and XPP measurements shown in Fig. 6(*c*) was deemed acceptable.

We have made additional observations of the performance of the LCLS HXSSS. The choice of the Hamamatsu Orca Flash4.0 CCD camera was driven by the need for high sensitivity for FEL low-charge operations. Its rolling shutter readout scheme led to the required 4 ms overall exposure time in order to expose all rows of the sensors during the arrival of the X-ray pulse. We discovered that whereas the Ce:YAG X-ray scintillation process has a well known lifetime of the order of a few nanoseconds, there was an additional and much-longer-timescale after-glow tail that extended well into the tens of milliseconds timescale. The end result was a weak 'ghost' spectrum of the previous pulse mixing with that of the current pulse. Although this artefact can be corrected by characterizing and performing a weighted subtraction, we plan to upgrade the camera to one with global shutter capabilities so the exposure time will be kept much shorter at tens of microseconds to minimize the effect of the long afterglow.

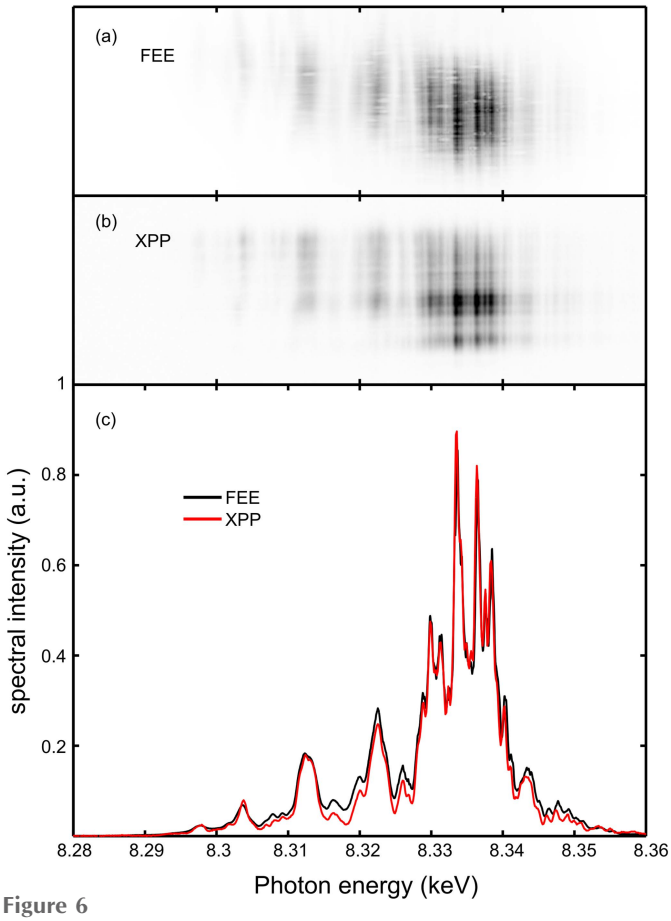

Figure 6
Comparison of simultaneously measured spectra in (*a*) the FEE and (*b*) the XPP instrument at 8.33 keV using the (220) reflection of a 20 µm Si crystal bent to 50 mm in radius. (*c*) Projections for the two measurements showing good agreement.

The damage threshold can be approached in the FEE for the silicon crystals due to its relatively high absorption cross section in the operating energy range of the HXSSS. For example, at 5 keV and for a 3 mJ pulse, the single-shot dose reaches a fraction of an eV atom^{-1}, resulting in instantaneous melting of the crystal. At 7 keV, when the machine was performing at an average 5 mJ pulse^{-1} levels, slow degradation of the crystal has been observed. Although moving the working area of the crystal to a fresh spot allows continuation of the operation, it is definitely an issue that must be addressed. Bent diamond crystals will be the easiest solution for mitigating the issue with instantaneous damage. Diamond has a lower absorption cross section than silicon and thus a higher damage threshold. In addition, a thicker crystal (20 µm *versus* 10 µm for Si for equal transmission) can be used for better mechanical rigidity. Furthermore, it was observed that there were FEL-induced vibrations in the thin silicon crystal because of the thermal–acoustic effect, which were quite long-lived and lasted over many milliseconds. Using a diamond thin crystal will help reduce significantly this vibration effect, which is particularly important for future high repetition rate FELs such as the European XFEL (http://www.xfel.eu) and the LCLS-II (https://portal.slac.stanford.edu/sites/lcls_public/lcls_ii/Pages/default.aspx). The only drawback is that diamond does not bend as easily as silicon because of its much higher Young's modulus. We are in the process of characterizing commercially available samples to see whether the crystal quality is sufficiently high and the required bending radius can be achieved.

4. Summary and conclusions

The engineering design considerations, implementation specifics, commissioning procedures, performances and additional findings of the new variable-energy HXSSS for the LCLS FEL are presented. The overall design utilized the concept of multiple crystal indices and multiple bending curvatures to cover a broad energy range with different resolution and bandwidth options. The combination of large NA optics, a high-sensitivity camera and the iris control, together contributed to a dynamic range of the spectrometer well beyond 10^6. A control interface has been developed to allow fine calibration of the device as well as turn-key operation. All mechanical motions and actuations were chosen to be external to the vacuum chamber to eliminate potential contamination concerns because of the close proximity of the system to the LCLS horizontal offset mirror system. All physics requirements including the operating photon energy range, spectral range and resolution were met by utilizing multiple surface cuts of silicon crystals and diffracting off different reflections to achieve optimal performances. The HXSSS can be operated from 4 to 20 keV, can work in a wide-spectral-range mode to map out the entire SASE spectrum of 0.5% or an even broader range to as much as 2%, and can achieve a resolution as high as 2×10^{-5} to resolve individual SASE spectral spikes or better when configured for high-resolution mode. Operational issues such as the Ce:YAG long-timescale after-glow as well as silicon being damaged by high-fluence FEL irradiation have been identified, and potential mitigations have been proposed.

Acknowledgements

Use of the Linac Coherent Light Source (LCLS), SLAC National Accelerator Laboratory, is supported by the US Department of Energy, Office of Science, Office of Basic Energy Sciences under Contract No. DE-AC02-76SF00515. The authors acknowledge support from the Hard X-ray Department of the LCLS during the commissioning of the HXSSS. The authors also recognize technical help and contributions from P. Montanez, J. Hastings, D. M. Fritz in development of the project.

References

Amann, J. *et al.* (2012). *Nat. Photon.* **6**, 693.
Bonifacio, R., Pellegrini, C. & Narducci, L. M. (1984). *Opt. Commun.* **50**, 373–378.
Brenner, G., Kapitzki, S., Kuhlmann, M., Ploenjes, E., Noll, T., Siewert, F., Treusch, R., Tiedtke, K., Reininger, R., Roper, M. D., Bowler, M. A., Quinn, F. M. & Feldhaus, J. (2011). *Nucl. Instrum. Methods Phys. Res. A*, **635**, S99–S103.

Feng, Y., Zhu, D., Feldkamp, J. M., Lemke, H. T., Robert, A., Fritz, D. M., Cammarata, M., Lee, S., Hastings, J. B. & Turner, J. L. (2012). *Proc. SPIE*, **8504**, 85040S.
Inubushi, Y., Tono, K., Togashi, T., Sato, T., Hatsui, T., Kameshima, T., Togawa, K., Hara, T., Tanaka, T., Tanaka, H., Ishikawa, T. & Yabashi, M. (2012). *Phys. Rev. Lett.* **109**, 144801.
Karvinen, P., Rutishauser, S., Mozzanica, A., Greiffenberg, D., Juranic, P. N., Menzel, A., Lutman, A., Krzywinski, J., Fritz, D. A., Lemke, H. T., Cammarata, M. & David, C. (2012). *Opt. Lett.* **37**, 5073.
Kondratenko, A. M. & Saldin, E. L. (1979). *Sov. Phys. Dokl.* **24**, 986.
Lutman, A. A., Decker, F.-J., Arthur, J., Chollet, M., Feng, Y., Hastings, J., Huang, Z., Lemke, H., Nuhn, H.-D., Marinelli, A., Turner, J. L., Wakatsuki, S., Welch, J. & Zhu, D. (2014). *Phys. Rev. Lett.* **113**, 254801.
Makita, M., Karvinen, P., Zhu, D., Juranic, P., Gruenert, J., Cartier, S., Jungmann-Smith, J. H., Lemke, H. T., Mozzanica, A., Nelson, S., Patthey, L., Sikorski, M., Song, S., Feng, Y. & David, C. (2015). *Optica*, **2**, 912.
Marinelli, A., Lutman, A. A., Wu, J., Ding, Y., Krzywinski, J., Nuhn, H.-D., Feng, Y., Coffee, R. N. & Pellegrini, C. (2013). *Phys. Rev. Lett.* **111**, 134801.
Rich, D., Zhu, D. & Feng, Y. (2012). *LCLS 8.4 keV fixed energy spectrometer.* Unpublished.
Rich, D., Zhu, D. & Feng, Y. (2013). *LCLS fixed energies spectrometer.* Unpublished.
Saldin, E. L., Schneidmiller, E. A. & Yurkov, M. V. (1998). *Nucl. Instrum. Methods Phys. Res. A*, **407**, 291–295.
Svetina, C., Abrami, A., Bacescu, D., Cudin, I., Fava, C., Gerusina, S., Gobessi, R., Rumiz, L., Sostero, G., Zangrando, M. & Cocco, D. (2011). *Proc SPIE*, **8139**, 81390J.
Wu, J. & Feng, Y. (2014). Unpublished.
Zhu, D., Cammarata, M., Feldkamp, J. M., Fritz, D. M., Hastings, J. B., Lee, S., Lemke, H. T., Robert, A., Turner, J. L. & Feng, Y. (2012). *Appl. Phys. Lett.* **101**, 034103.
Zhu, D., Cammarata, M., Feldkamp, J., Fritz, D. M., Hastings, J., Lee, S., Lemke, H. T., Robert, A., Turner, J. & Feng, Y. (2013). *J. Phys. Conf. Ser.* **425**, 052033.